CFD Study of Fluid Flow and Wall Heat Transfer in a Fixed Bed of Spheres

Michiel Nijemeisland and Anthony G. Dixon
Dept. of Chemical Engineering, Worcester Polytechnic Institute, Worcester, MA 01609

DOI 10.1002/aic.10089
Published online in Wiley InterScience (www.interscience.wiley.com).

A study is presented of the relationship between the local flow field and the local wall heat flux in a packed bed of spheres. Computational fluid dynamics is used as a tool for obtaining the detailed velocity and temperature fields, for gas flowing through a periodic wall segment test cell. Results from the wall segment are demonstrated to reproduce those obtained from a full bed of spheres with tube-to-particle diameter ratio of $N = 4$. Attempts to correlate the local wall heat flux with local properties of the flow field, such as velocity components, velocity gradients, and components of vorticity, led to the conclusion that local heat transfer rates do not correlate statistically with the local flow field. Instead, a conceptual analysis was used to suggest that local patterns of wall heat flux are related to larger-scale flow structures in the bed. © 2004 American Institute of Chemical Engineers *AIChE J,* 50: 906–921, 2004

Keywords: fixed bed, computational fluid dynamics, heat transfer, flow through sphere packs, wall effects

Introduction

Fixed-bed reactors are used in many different chemical processes and are a very important part of the chemical industry. To model fixed beds, we must have a good qualitative understanding and an accurate quantitative description of their fluid flow and heat transfer. Fixed-bed models have usually been developed for high tube-to-particle diameter ratio (N) beds, where temperature and flow profile gradients are mild and can be averaged. Modeling of the low-N beds ($3 \leq N \leq 8$), used in extremely exo- and endothermic processes in tube-and-shell type reactors, is complicated because of the presence of wall effects across the entire radius of the bed. Heat transfer is one of the most important aspects. To obtain accurate models of heat transfer, we need to study its dependency on realistic flow features in these low-N beds.

Recently, the range of applications for computational fluid dynamics (CFD) has been extended to the field of chemical engineering with the introduction of specially tailored fluid mixing programs. The general setup of most CFD programs allows for a wide range of applications, and several commercial packages have introduced chemical reactions into the CFD code, allowing rapid progress of the use of CFD within the field of chemical reaction engineering (Bode, 1994; Harris et al., 1996; Kuijpers and van Swaaij, 1998; Ranade, 2002). Already, CFD can be applied to the more physical aspects of chemical engineering, cases in which heat transfer and mass flow are the essentials.

In the field of fixed-bed modeling, there are two different types of models referred to by the term "CFD simulation." In the first, the bed is represented as an effective porous medium, with lumped parameters for dispersion and heat transfer (Jakobsen et al., 2002). The reactions that take place in the porous catalyst particles are represented by source or sink terms in the conservation equations (Ranade, 2002) and corrected for volume fraction and particle transport limitations. The velocity field can be obtained from a modified momentum balance (Bey and Eigenberger, 1997) or a form of the Brinkman–Forcheimer-extended Darcy equation (Giese et al., 1998). These approaches provide an averaged velocity field, usually in the form of a radially varying axial component of velocity, which is an improvement over the classical assumption of plug flow (con-

Correspondence concerning this article should be addressed to A. G. Dixon at agdixon@wpi.edu.

stant unidirectional flow). These velocity fields have been used in improved models of fixed-bed transport and reaction (Winterberg et al., 2000). The disadvantages of this approach have been the continued lumping of transport processes, thus obscuring the physical basis of the model, and the necessity of introducing an effective viscosity for the bed, to bring computed and experimental velocity profiles into agreement (Bey and Eigenberger, 1997; Giese et al., 1998).

In the second type of CFD fixed-bed simulation, the geometrical complexities of the packing are not simplified, or replaced, by the effective medium that is used in the first approach. The governing equations for the fluid flow itself are relatively simple, however, the geometric modeling and grid generation become complicated and the computational demands increase significantly (Ranade, 2002). Because of the computational requirements, the approach can so far be applied only to small, periodic regions of the reactor. It is therefore useful mainly as a learning tool, from which we can develop detailed insight into fixed-bed flow structures, and understand how they influence transport and reaction. The understanding from this more rigorous "discrete particle" CFD can then be used to inform the simplifying decisions made for the more computationally tractable "effective medium" CFD simulations.

Earlier work on discrete particle simulations of fixed beds has been reviewed recently (Dixon and Nijemeisland, 2001). Sørensen and Stewart (1974) studied particle-to-fluid heat transfer under creeping flow in a three-dimensional (3-D) cubic array of spheres. Dalman et al. (1986) investigated flow behavior in an axisymmetric radial plane with two spheres, giving a first high-detail insight into flow patterns in fixed beds. This study showed that eddies could form between the spheres, which led to a region of poor heat transfer. Lloyd and Boehm (1994) did a very similar 2-D study with eight instead of two spheres in line. In this study the influence of the sphere spacing on the drag coefficients was investigated. It was also found that heat transfer from the spheres decreased with decreased sphere spacing. McKenna et al. (1999) obtained valuable insight into the effect of particle size on particle–fluid heat transfer from a 2-D CFD study of small clusters of catalyst particles and a single catalyst sphere close to a wall.

Earlier studies in our group used a 3-D three-sphere model (Derkx and Dixon, 1996), followed by an eight-sphere model (Logtenberg and Dixon, 1998a,b) in which the packing was modeled as two layers of four spheres, perpendicular to the flow in the tube with a tube-to-particle diameter ratio, $N = 2.43$. Subsequently, a 3D 10-sphere model was developed, with $N = 2.68$, incorporating contact points between the particles and between the particles and the wall (Logtenberg et al., 1999). These studies focused on using CFD to obtain traditional heat transfer modeling parameters such as the wall Nusselt numbers (Nu_w), and gave reasonable qualitative agreement with experimental estimates.

Several other groups have studied fluid flow in discrete particle beds. Esterl et al. (1998) and Debus et al. (1998) applied a computational code by Nirschl et al. (1995) to find flow profiles, using an adapted chimera grid. This grid consisted of a structured grid, based on the flowing medium, which was overlaid by a separate structured grid, based on the packing particles. Calculated pressure drops were compared against predicted pressure drops using, among others, Ergun's relation for a bed with the same porosity; the simulation data gave the same order of magnitude. Simulations were performed in beds with up to 300 spheres, although the bed for which results were discussed consisted of 120 spheres. One of the aspects that may have affected the accuracy of the simulations is that the bed was only approximately five layers deep, resulting in a flow that mainly consisted of inlet and outlet effects.

Other research groups have used commercial CFD packages to simulate behavior in fixed beds. Calis et al. (2001) applied the commercial code CFX-5.3 to a structured packing of spheres. They simulated flow in a number of channels of square cross section filled with spherical particles. Several different types of structured packings were investigated, all based on structured packing of spheres. The repetitive sections had varying values of N, from 1 to 4. Values for pressure drop obtained from the simulations were validated against experimental values. The turbulence models used (κ-ε and RSM) showed similar results, with an average error from the experimental values of about 10%. Pressure drop in a structured packing was also studied by Petre et al. (2003), who used the CFD results to construct submodels of different contributions to the overall pressure drop.

Still other research groups (Georgiadis et al., 1996; Maier et al., 1998; Manz et al., 1999; Suekane et al., 2003; Zeiser et al., 2001) used a lattice Boltzmann technique for simulation of flow in a fixed bed of spheres. A dense packing of spheres in a cylindrical column was created from experimental observations, such as magnetic resonance imaging (MRI), or by computer simulation, using a raining and compression algorithm. The created packing topology was then divided into an equidistant Cartesian grid, where individual elements were labeled as solid or fluid regions as in a marker-and-cell approach. A high resolution of the grid made it possible to obtain accurate flow profiles. Recently (Freund et al., 2003; Yuen et al., 2003; Zeiser et al., 2002) simple reactions have been added to the simulation, showing species and conversion profiles inside the bed.

The main limitation of the lattice Boltzmann technique is that it cannot handle energy balances as of yet. Incorporating heat transfer into fixed-bed simulations is extremely challenging, given the need to mesh and solve both flow in the voids and conduction in the particles. Following the earlier work on cubic packings or simplified clusters of a small number of particles, CFD simulations of flow in more extensive fixed beds have all been isothermal. The contribution of the present work is to present the use of CFD to add heat-transfer modeling to calculations of flow near the tube wall of a fixed bed of spheres.

CFD Methodology

Computational fluid dynamics (CFD) codes make it possible to numerically solve flow, mass, and energy balances in complicated flow geometries, such as a packed bed. The differential forms of these balances are applied to a large number of control volumes, which together make up the computational domain. The size and number of control volumes (mesh density) are user determined and will strongly influence the accuracy of the solutions. After boundary conditions have been implemented, the flow and energy balances are solved by an iteration process that decreases the error in the solution until a satisfactory result has been reached.

One of the most important parts of CFD modeling is the construction of the mesh topology. In our earlier studies (Derkx and Dixon, 1996; Logtenberg and Dixon, 1998a,b; Logtenberg et al., 1999) the mesh density was investigated extensively. Additional studies were done to find the optimal mesh density, for the specific simulation geometries used here. Fluent UNS Version 5.4 was used, which is based on unstructured meshes to allow flexibility for the complex geometry of a fixed-bed packing. The simulations were mostly performed on a Dell workstation with dual P III Xeon 1.0 GHz processors, and 2 GB of RAM. The large amounts of RAM were necessary to handle the complex geometries that were used. Some of the runs were made on a more recently acquired Dell workstation with a P III Xeon 1.4 GHz processor and 4 GB of RAM.

The general equations used for conservation of mass (the continuity equation), conservation of momentum, and conservation of energy, and the finite volume method used to discretize them are all described in standard references for the subject (Patankar, 1980). In the present application, particular care was given to the choice of turbulence model, and to the treatment of flow near solid surfaces.

Turbulence

The Renormalization Group (RNG) κ-ε model (Yakhot and Orszag, 1986) was used for the turbulence conditions in the CFD simulations. The major differences, in application, from the standard κ-ε model are different empirical constants in the κ and ε balances and extra terms in the turbulent dissipation balance (ε). The RNG methods are a general methodology of model building based on the stepwise coarsening of a problem. The main idea is that the RNG theory is applicable to scale-invariant phenomena that do not have externally imposed characteristic length and time scales. In the case of turbulence, the RNG theory is applicable to the small-scale eddies, which are independent of the larger-scale phenomena that create them.

The form of the main balances in the RNG κ-ε model are similar to the balances in the standard κ-ε model, with the modification from the RNG statistical technique (Fluent, Inc., 1997). The momentum equation is derived to be

$$\frac{\partial(\rho u_i)}{\partial t} + \frac{\partial(\rho u_i u_j)}{\partial x_j} = -\frac{\partial p}{\partial x_i} + \frac{\partial}{\partial x_j}\left[\mu_{eff}\left(\frac{\partial u_i}{\partial x_j} + \frac{\partial u_j}{\partial x_i}\right)\right] \quad (1)$$

The effective viscosity in this balance is computed using the form of a high Reynolds number. This is identical to the turbulent viscosity defined in the standard κ-ε model

$$\mu_t = \rho C_\mu \frac{\kappa^2}{\varepsilon} \quad (2)$$

The only difference lies in the constant C_μ, which is 0.09 in the standard κ-ε model and 0.0845 in the RNG κ-ε model.

The transport equations for the turbulent kinetic energy κ and the turbulence dissipation ε in the RNG κ-ε model are defined similarly, now using the effective viscosity defined through the RNG theory. A mean strain rate, S, is used instead of separate turbulence source terms

$$\frac{\partial(\rho\kappa)}{\partial t} + \frac{\partial(\rho u_i \kappa)}{\partial x_i} = \frac{\partial}{\partial x_i}\left(\alpha_\kappa \mu_{eff}\frac{\partial \kappa}{\partial x_i}\right) + \mu_t S^2 - \rho\varepsilon \quad (3)$$

and

$$\frac{\partial(\rho\varepsilon)}{\partial t} + \frac{\partial(\rho u_i \varepsilon)}{\partial x_i} = \frac{\partial}{\partial x_i}\left(\alpha_\varepsilon \mu_{eff}\frac{\partial \varepsilon}{\partial x_i}\right) + C_{1\varepsilon}\frac{\varepsilon}{\kappa}\mu_t S^2 - C_{2\varepsilon}\rho\frac{\varepsilon^2}{\kappa} - R \quad (4)$$

where α_κ and α_ε are the inverse effective Prandtl numbers for κ and ε, respectively. The model constants $C_{1\varepsilon}$ and $C_{2\varepsilon}$ from Eq. 4 are derived analytically through the RNG theory and are, respectively, 1.42 and 1.68 (in the standard κ-ε model these model constants are 1.44 and 1.92, respectively).

The major difference in the RNG κ-ε model from the standard κ-ε model can be found in the ε balance, where a new source term appears in the R term. This term is a function of both the turbulent kinetic energy κ and the turbulence dissipation term ε. The R term in the RNG κ-ε model makes the turbulence in this model sensitive to the mean rate of strain. This results in a model that is responsive to effects of strain and streamline curvature, a feature that is nonexistent in the standard κ-ε model. The inclusion of this effect makes the RNG κ-ε model more suitable for complex flows, such as flow in fixed beds, in which the streamlines must curve around the particles.

Energy

The RNG model provides its own energy balance, which is based on the energy balance of the standard κ-ε model. The RNG κ-ε model energy balance is defined as a transport equation for enthalpy, as follows

$$\frac{\partial(\rho h)}{\partial t} + \frac{\partial(\rho u_i h)}{\partial x_i} = \frac{\partial}{\partial x_i}\left(\alpha c_p \mu_{eff}\frac{\partial T}{\partial x_i}\right) + \frac{Dp}{Dt} + (\tau_{ik})_{eff}\frac{\partial u_i}{\partial x_k} + S_h \quad (5)$$

where h is the sensible enthalpy, τ_{ik} is the deviatoric stress tensor and α is the inverse turbulent Prandtl number for temperature. In the traditional turbulent heat transfer model, the Prandtl number is fixed and user-defined; the RNG model treats it as a variable dependent on the turbulent viscosity. It was found experimentally that the turbulent Prandtl number is indeed a function of the molecular Prandtl number and the viscosity (Kays, 1994).

Wall functions

To be able to resolve the flow solution near solid surfaces with zero flow boundary conditions, there need to be some special conditions set. Besides the zero flow boundaries, the presence of a solid surface also affects the turbulence; the dissipation of turbulent kinetic energy (ε) is much larger near a solid surface because the turbulence is damped. Slightly further away from the solid surface, still in the boundary layer,

there is a source of turbulent kinetic energy atributed to the local Reynolds stresses and the large gradient of the mean velocity. Several methods are available to resolve both the zero flow condition at the solid surface and the turbulent conditions near the solid surface. The most fundamental is to directly resolve the boundary layer, using a highly refined mesh close to the solid surface. In a fixed-bed model, where there is so much solid surface from both tube wall and packing, this approach would be prohibitively expensive in computational resources.

The general goal of the wall function approach is to replace the direct modeling of the viscous sublayer and the transition region to the fully turbulent layer with one empirical model, in effect linking the solution variables in the cells adjacent to the solid surface to the corresponding values on the solid surface. In our simulations we have used two different wall function models, the standard wall function and the nonequilibrium wall function.

The standard wall function is based on a proposal by Launder and Spalding (1974), and it has been used widely for industrial flows. The wall function describes the velocities, temperatures, and turbulent quantities in the region close to the wall. The nonequilibrium wall function (Kim and Choudhury, 1995) is the most suitable for complex flows involving separation, reattachment, and impingement where the mean flow and turbulence are subjected to severe pressure gradients and change rapidly. In such flows, improvements can be obtained, particularly in the prediction of wall shear and heat transfer. In the nonequilibrium wall function approach the heat-transfer procedure remains exactly the same. The mean velocity is made more sensitive to pressure gradient effects.

Validation study

Because the CFD methodology is not specifically designed for application in constrained geometries, such as particle packed beds, it was necessary to verify whether the simulated results were valid. Although the CFD code is based on fundamental principles of flow and heat transfer, some of the boundary issues were modeled using empirical data not necessarily appropriate for the fixed-bed application.

A 44-sphere model was created with $N = 2$ (Nijemeisland and Dixon, 2001). This specific geometry was used to validate CFD results in fixed beds by comparing radial temperature profiles of the simulations with experimental data in an identical setup. The comparisons showed that experimental temperature profiles and CFD-produced profiles were qualitatively and quantitatively comparable, although several adjustments to the final temperature profiles of both the experimental results and the CFD simulation were needed to compensate for deviations in the measurements and simulations. Factors that were adjusted included thermal conduction through the thermocouple cross for the experimental results and radiation effects and solid–solid conduction that were neglected in the CFD simulations.

The direct comparison of the temperature profiles acquired experimentally and from the CFD simulation showed that when CFD is applied to fixed-bed analysis it gives identical, though more detailed, results compared to those by experimental data acquisition. CFD can be considered a new method of data acquisition in fixed beds. This new method requires a considerable amount of work to set up, although once operational provides a wealth of data unavailable through any other method.

Simulation of Full Diameter Tube

Industrial application of low tube-to-particle diameter ratio beds starts at about $N = 4$ to 8, depending on the process. Our previous work focused on the validation study of an $N = 2$ bed (Nijemeisland and Dixon, 2001). The value $N = 2$ was chosen to allow the construction of an experimental setup and a CFD model that had identical geometry, as far as possible. We were able to simulate the full length of the experimental tube for $N = 2$ using a model with 44 spheres. In the present work, as a representation of a larger N bed, a CFD model with $N = 4$ was chosen because geometric data for this case were already available and it was of interest as one of the standard values for N in steam reforming.

Experience in CFD modeling of fixed beds in tubes has taught us that the number of control volumes increases rapidly with increasing N, and linearly with increasing bed length. A full industrial $N = 4$ bed has approximately 12 spherical particles in a cross section, is approximately 13 meters in length, and a full simulation of this was estimated to consist of about 7200 particles. To be able to solve for certain details in the model, such as areas where particles in the packing touch each other, or the tube wall, a high level of detail is necessary for the required accuracy of the simulation. More particles in a geometry will lead to more high-detail areas, thus increasing the computational size of the geometry very quickly. The computational grid for this bed, at the desired mesh density, would consist of approximately 600 million control volumes. Such large computational grids are currently unmanageable, both in grid size and in the iteration process.

From these considerations the need to limit the simulation geometry was apparent. The largest simulation geometry reduction can be obtained by imposing axially translational periodic boundaries. By using these periodic boundaries only a section of the entire bed needs to be modeled; additionally the effects of inlet and outlet boundary conditions are removed. To implement these conditions, the structure of the $N = 4$ bed had to be obtained and analyzed.

It was initially attempted to determine the structure of the bed experimentally. Both wax models that could be cut into slices, and transparent acrylic spheres in a Plexiglas tube that allowed digital photography, were used. After determining the positions of the spheres, the structure of the bed had to be implemented as a computational geometry. For this the positions of the spheres had to be established very precisely. Satisfactory results could not be obtained by the experimental methods because of the unavoidable uncertainties in the sphere positions introduced by the measurements.

The low tube-to-particle diameter ratio of the model ensured a relatively regular structure in the bed and made it possible to refine the experimentally obtained sphere locations using geometric relations. The experience gained during the experimental analyses led to the observation that the packing structure away from the support plate consisted of two intertwined regular substructures, a wall layer consisting of layers of nine spheres and a central structure consisting of a three-sphere spiraling repetitive structure. Similar observations of a wall layer and a central region have been made in studies of com-

puter-generated packings (Mueller, 1997). The spiral nature of the structure necessitated six packing layers for the central spheres to return to their original positions, so that periodic boundary conditions on the flow could be accommodated. The final full-bed model was constructed with the six layers and 72 spheres in total.

With the model geometry established, the discretization mesh for the finite-volume method had to be created. Our previous experience (Nijemeisland and Dixon, 2001) had demonstrated that at the particle–particle and wall–particle contact points, the mesh became extremely distorted. This resulted in the failure of the numerical method under turbulent flow conditions, which was believed to be connected to the use of the wall functions. Following our previous strategy, all spheres were reduced to 99% of their original size after placement. This method creates small gaps at the contact points of the spheres with each other and the wall. The additional fluid regions that were created were shown to have no influence on the flow solution, and a small and correctable influence on the heat transfer (Nijemeisland and Dixon, 2001).

For a more accurate solution, a finer mesh size is required. However, this leads to higher computational requirements. In our model, the control volumes generated by the mesh need to be at least as small as the wall–particle gaps. In the larger void areas, the control volumes may be bigger. When the full-bed model, including the internals of the particles, was created using control volumes with the size of the gaps, the total number of control volumes came to approximately 47 million, which was clearly far too high for practical computation. A graded mesh was created next, using a fine mesh near the contact areas and a coarser mesh in the larger voids of the bed and inside the spheres. This resulted in a total of six million control volumes. This mesh also could not be used because of software restrictions, and it was necessary to restrict full-bed modeling with the graded mesh to the fluid region only. The full-bed simulation geometry and some details of the graded mesh on the sphere surfaces can be seen in Figure 1. In particular, the mesh refinement near the contact points is clearly seen. Only fluid flow could be solved using the graded mesh on the fluid region. To accommodate heat transfer, a coarser mesh for both fluid and solid regions was created. The full-bed flow results from the coarser mesh could be compared to those from the finer, graded mesh. These results are presented as part of the full-bed/wall segment comparison in the next section.

Figure 1 also shows the periodic nature of the model geometry. In a periodic boundary model the inlet and outlet plane geometries are identical and the flow conditions are set to be identical as well. This effectively imposes the outlet conditions of the bed section on the inlet, and therewith establishes the translational periodic condition and creates a model of a generic section in the bed. We have presented some laminar, isothermal flow solutions using a coarse mesh for the $N = 4$ bed in an earlier paper (Dixon and Nijemeisland, 2001). In the present work, our focus is on the added complication of heat transfer.

When a nonisothermal bed is to be simulated, the temperature profile develops along the bed axial coordinate, and the temperature field is not periodic. To use the periodic flow boundary conditions, the momentum and energy balances must be decoupled and the flow parameters, such as viscosity and density, must be assumed independent of temperature. An isothermal, periodic flow solution is calculated first, then the resulting velocity field is taken as fixed during the solution of the energy balance. The flow inlet and exit boundaries are set as a velocity inlet and a pressure outlet, although the flow parameters in these boundary conditions are not used at this point.

To calculate the development of the temperature profile in the bed, a series of simulations has to be performed. In the series of simulations the generic sections are virtually stacked by imposing the outlet temperature conditions of one section as the inlet conditions of the downstream section. In this approach, axial conduction cannot be included because there is no mechanism for energy to transport from a downstream section back to an upstream section. Thus, this method is limited to reasonably high flow rates for which axial conduction is negligible compared to the convective flow of enthalpy.

To create a complete picture of the developing profile the resulting temperature contour maps of the different stages can be placed together. Figure 2 shows the result of placing the temperature maps of four consecutive simulations together. The two pictures, for $x = 0$ and $y = 0$, correspond to two sections through the length of the tube, at right angles to each other. In these pictures, the main axial flow is from left to right, and $\mathrm{Re}_p = 1000$. This value of Re_p was used for all subsequent simulations. An initial temperature of 300 K was taken for the inlet of the first stage, and the wall temperature was constant at 400 K. The fluid properties were those of air, giving a Prandtl number of approximately $\mathrm{Pr} = 0.7$, and the particle properties were those of alumina. The simulation therefore corresponds to a typical laboratory heat transfer experiment setup, in which the tube wall is heated by a steam jacket, for example, and energy is transferred from the wall into the colder flowing fluid.

The overall picture of the temperature field presented in Figure 2 confirms our intuitive expectation of a classical "boundary-layer" type of development, with a colder inner core and a warmer near-wall region. Closer inspection shows that the boundary layers are, in fact, interrupted by the presence of the particles. These are not isothermal, despite their higher thermal conductivity, yet the temperature field within a particle differs from that in the surrounding fluid. Fingers of warmer fluid infiltrate between the particles as flow is deflected radially. The behavior of local heat transfer rates, and of catalyst particles situated in these temperature fields, will depend on the local temperature and flow conditions, which are difficult to isolate in the larger view.

There is a slight discontinuity in the temperature contours between the sections, most noticeably between the first and second sections. This is related to the neglect of axial conduction between stages mentioned above. This is not evident in the fluid phase, given that axial conduction through the fluid is small compared to the convective transport. In the solid phase, however, back-conduction from the warmer second stage results in a higher temperature at the stage entrance because there is no heat flux between the stages in the solid phase.

The simulation of full beds, even for $N = 4$, is difficult and computationally demanding, resulting in an enormous amount of information that also presents problems in data reduction. This leads to the conclusion that we need a model focusing on a small number of catalyst particles near the wall of the tube, and their direct neighbors, for an accurate description of the

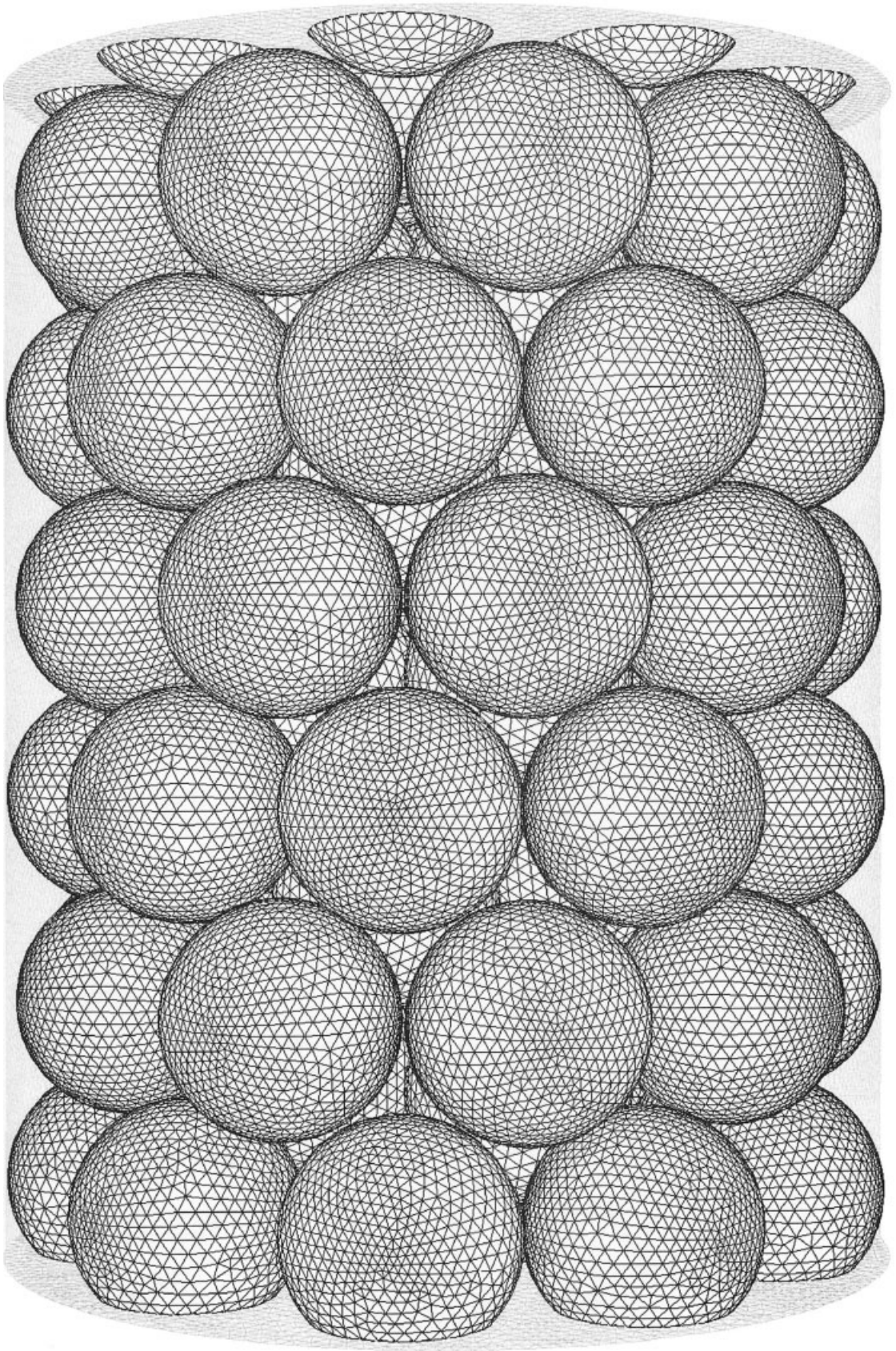

Figure 1. $N = 4$ full bed simulation geometry.

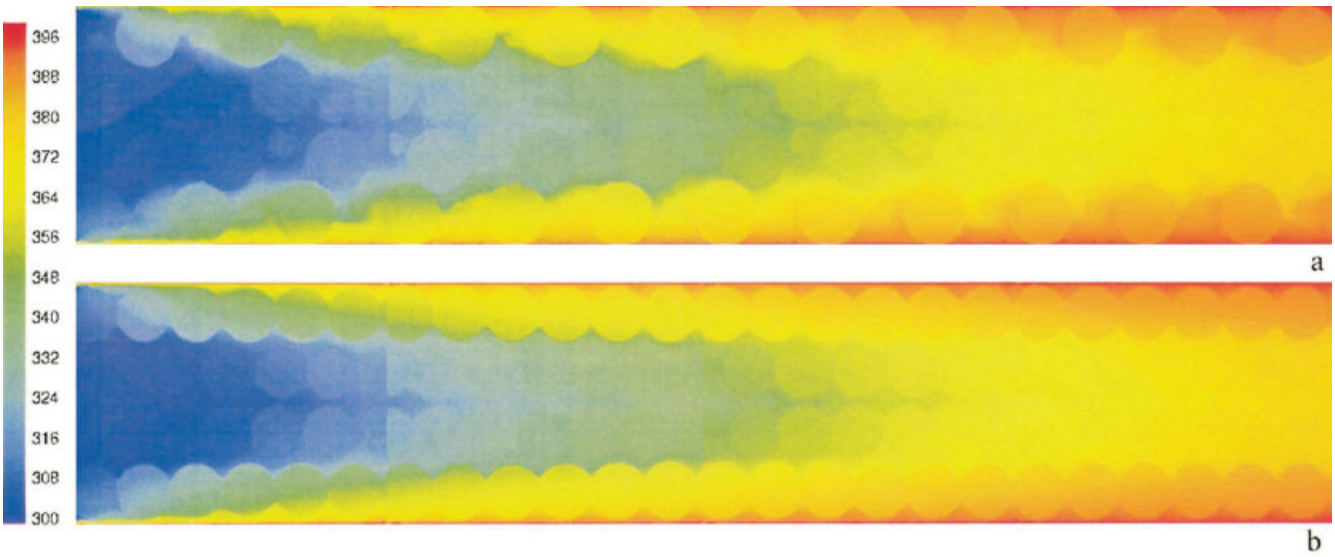

Figure 2. Continuous temperature profiles in the (a) $y = 0$ and (b) $x = 0$ planes for four stacked simulations geometry segments.

heat transfer and flow processes taking place on a local scale. The near-wall region is the most interesting area because this is where the largest heat transfer gradient occurs.

Wall Segment Model

Simulations of heat transfer in fixed beds of discrete particles place severe demands on computational resources. The basic problem is the need to mesh the particles, to allow for solid conduction. Although a relatively coarse mesh would probably be sufficient inside the particles, the internal particle mesh is dictated by the surface mesh; in turn, this is governed by the need for compatibility with the mesh in the fluid adjacent to the particle. That mesh, however, has to be very fine to properly represent flow near the particle–particle contact points, even with the use of near-wall models.

To be able to obtain accurate enough results for specific regions in the bed simulation, or to be able to simulate a specific region faster, a reduced-size model can be created of a segment of the overall simulation model. Because our primary concern is to find the influence of flow patterns on the wall heat transfer, the near-wall region is the logical section on which to focus. This segment geometry can be used to generate simulation results more quickly because of its limited size. This requires the addition of several new boundaries on which appropriate boundary conditions have to be implemented.

We have chosen to focus on a 120° "slice" of the bed cross-sectional area, as illustrated in Figure 3. A single-particle layer of the segment contains a fully symmetrical layout of particles, including three wall spheres and one center sphere. Because in the full bed six layers were necessary to create periodic conditions, because of the spiral nature of the three center spheres, six layers would also be needed for the segment model. This would, however, defeat the purpose of creating a segment model, that is, reduction of model size. It was therefore chosen to slightly adjust the positions of the central spheres, to allow for periodic boundary conditions over two layers of spheres, as shown in Figure 3. For a wall-segment model, periodic boundary conditions on the top and bottom boundaries are necessary, and a layout that allows for these conditions, as well as the symmetry conditions on the side walls of the segment, is needed.

When simulations are done in a reduced wall-segment model the results need to be validated against a full-bed model. The main reason for this is to see whether the wall-segment model results are representative for a full bed, following the adjustment of the center spheres, and also to check that the boundaries, which are relatively close to all parts of the segment model, do not influence the solution.

As mentioned in the previous section, a fine graded mesh was developed for the full-bed model, although it was impossible, because of memory restrictions, to export the completed mesh to the simulation program. It was possible to create a fine graded mesh for the fluid region alone, that is, when all solid parts (the particle internals) were excluded from the mesh. This mesh required 2.6 million control volumes. Only flow simulations could be performed with this mesh. A coarser mesh was also developed for the full bed that included both particles and fluid, on which both flow and energy analyses could be performed. The full-bed coarse mesh consisted of 1.97 million control volumes, three times smaller than the fine graded mesh. Similarly, for the wall-segment model, both a fine graded mesh and a coarse mesh were created. The difference is that for the segment the fine graded mesh could be applied to both particles and fluid, giving approximately 760,000 control volumes. This is the mesh that is shown in Figure 3, on the particle surfaces and on the bottom periodic boundary. The coarse mesh was at a similar resolution to the coarse mesh developed for the full bed, and was used for comparison purposes only.

Wall-segment flow and energy runs were made under the same conditions as for the full-bed runs. Wall-segment results were compared to full-bed results, for the simulated flow fields. Additionally, mesh independence studies were performed on the full-bed model and the wall-segment model. The results of the different simulations were directly compared using radial

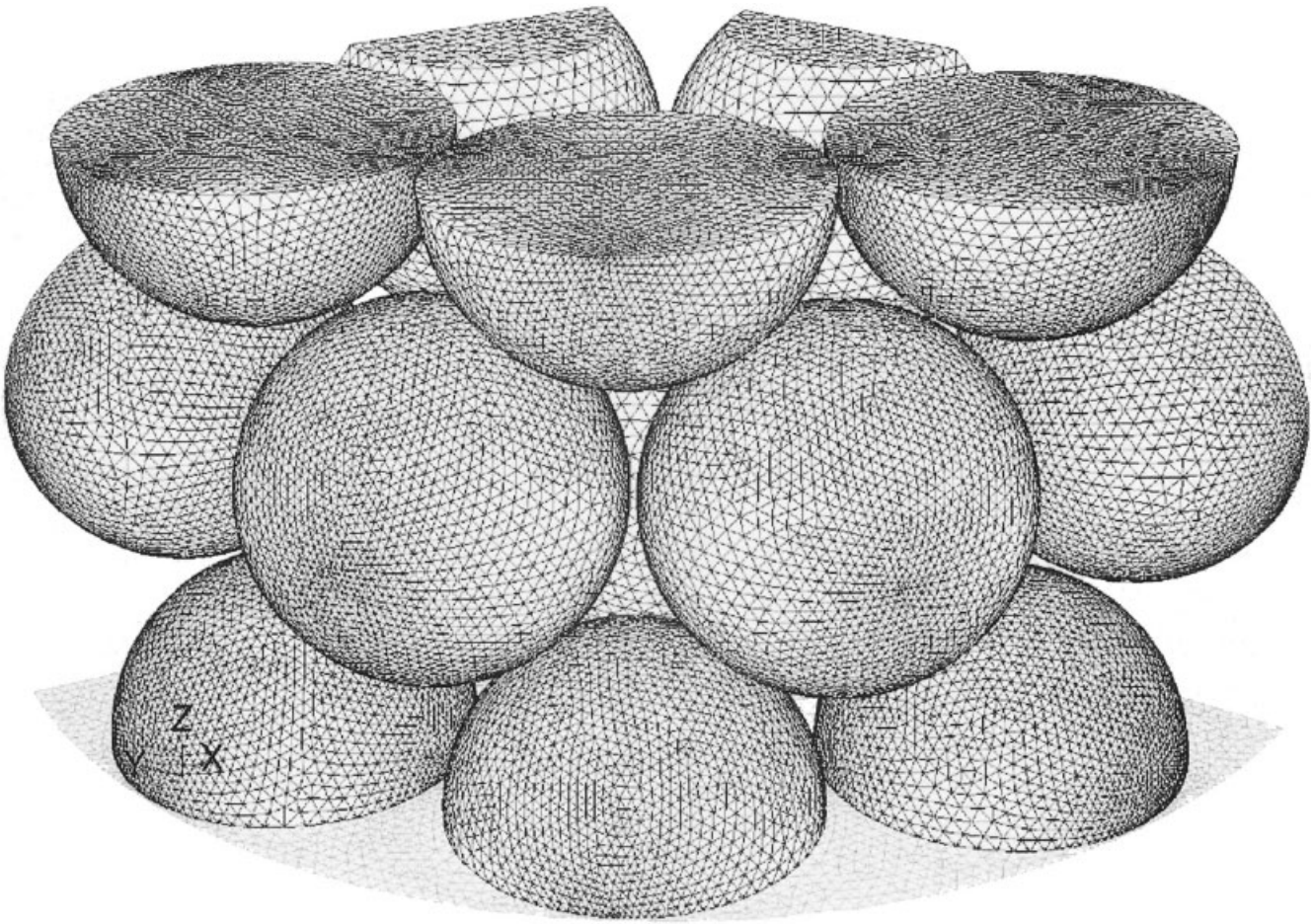

Figure 3. Wall segment simulation geometry.

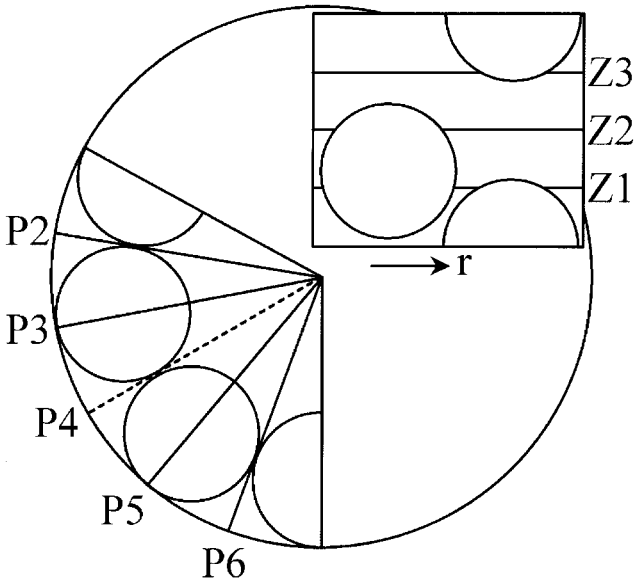

Figure 4. Planes P2 through P6 indicated in the wall segment geometry, and axial positions Z1, Z2, and Z3 indicated in plane P4.

velocity profiles sampled from various predefined locations, indicated in Figure 4. These were located on five axial planes at different angular positions, labeled P2 through P6, at three different axial positions, Z1 through Z3, shown in the inset to Figure 4. The comparisons presented here were obtained from plane P4 because it was furthest removed from the effects of the symmetry boundaries, at each of the three axial positions.

The overall flow field in plane P4, from which the radial velocity profiles were obtained, is shown in Figure 5, as a velocity vector plot. The velocity magnitude is represented by both the size of the arrows and their color, as given in the scale. This simple planar representation of the flow field shows regions of reversed flow in the wake of the particles, as well as recirculating wake flow near the contact points of particles. Near the bottom of the particle in the top right of the plot a fairly strong radial flow can be identified. Similar features were identified previously (Dixon and Nijemeisland, 2001).

The axial component of velocity was made dimensionless using the inlet average velocity v_{in} and is shown in Figure 6. The figure compares profiles at three axial positions in the plane P4. In this figure, two comparisons are being made simultaneously. The fine and coarse meshes for the full-bed flow simulations are compared, to check that the flow results are independent of mesh density. In addition, the wall-segment and the full-bed models are compared at the same mesh density.

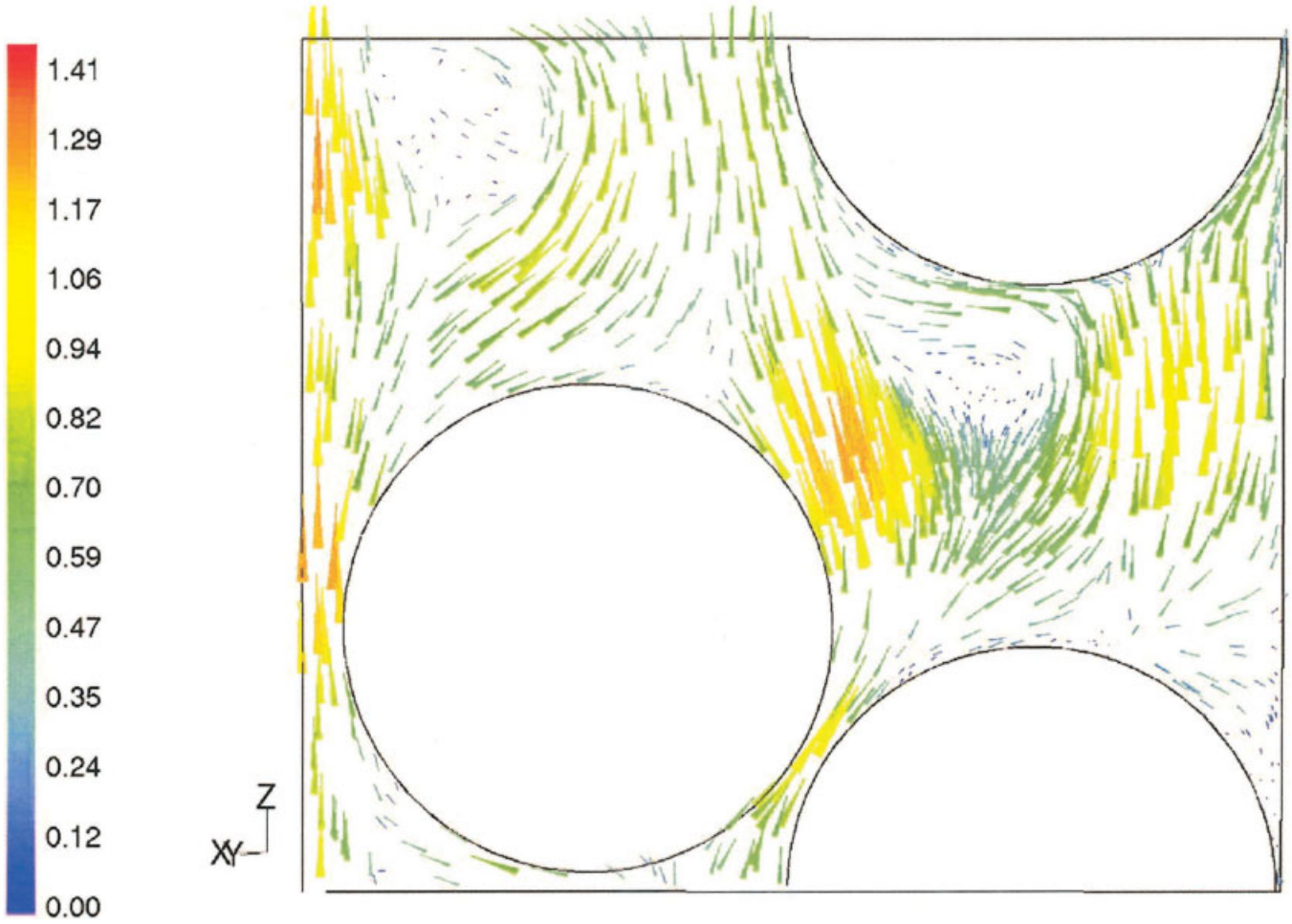

Figure 5. Velocity vector plot of plane P4; vectors are colored by velocity magnitude in m/s.

The velocity profile plots show interruptions in the velocity profile, which is where solid particles were located, so that no velocity data were available. In general, the data of the three different cases agree very well qualitatively: velocity highs and lows are shown at the same points in the bed. Quantitatively, the results of the two full-bed models are practically identical, indicating that the solutions were completely mesh independent. The data from the wall-segment model in some cases deviate slightly from the full-bed models. This can be explained by the slightly different layout of the wall-segment model center spheres, as explained above. The differences in velocity magnitudes are mainly found in the transition area between the wall spheres and the central spheres. The effect of slightly larger gaps between spheres from the nine-sphere wall region and the three-sphere central region, attributed to the sphere relocations, has an effect on the magnitude of the velocity profile. Some differences are also found in the central layer area where the sphere positions are not identical. Agreement is generally excellent in the region of most concern to us, near the wall. Similar plots were made for the radial and tangential components of velocity, with essentially the same results.

A second series of axial velocity component radial flow profile comparisons is shown in Figure 7. Again, two comparisons are made in this figure. The effect of mesh density for the wall segment was investigated using the fine graded mesh (labeled "wall-segment" in the figure) and the coarse mesh. We also wanted to investigate whether the scale of the model affected the results. This might be expected if the small-scale turbulence were important in our results, in that this scale would be independent of the model scale, and would play a different role if the model scale were changed. A simulation geometry was created at 1/8th the size of the original model, to see whether the absolute size of the model had a significant influence on the solution of the physical models, including the wall functions, which resolve the wall boundary layers. To scale down the simulation geometry, a linear factor of 0.125 was used, creating a wall segment of 1/512th the volume of the original model, using the fine graded mesh. The fluid velocity was also scaled down to maintain the same value of Reynolds number. It was reasoned that if the physical models were resolved properly, there should be minimal difference between the flow profiles. The only regions in which some differences were expected were near surfaces, where the effect of the no-slip boundary may have been more pronounced in the smaller geometry.

The dimensionless axial component of velocity is compared in Figure 7 at the same positions as for the comparisons in Figure 6. The results in Figure 7 show no significant differences, either qualitatively or quantitatively, between the pro-

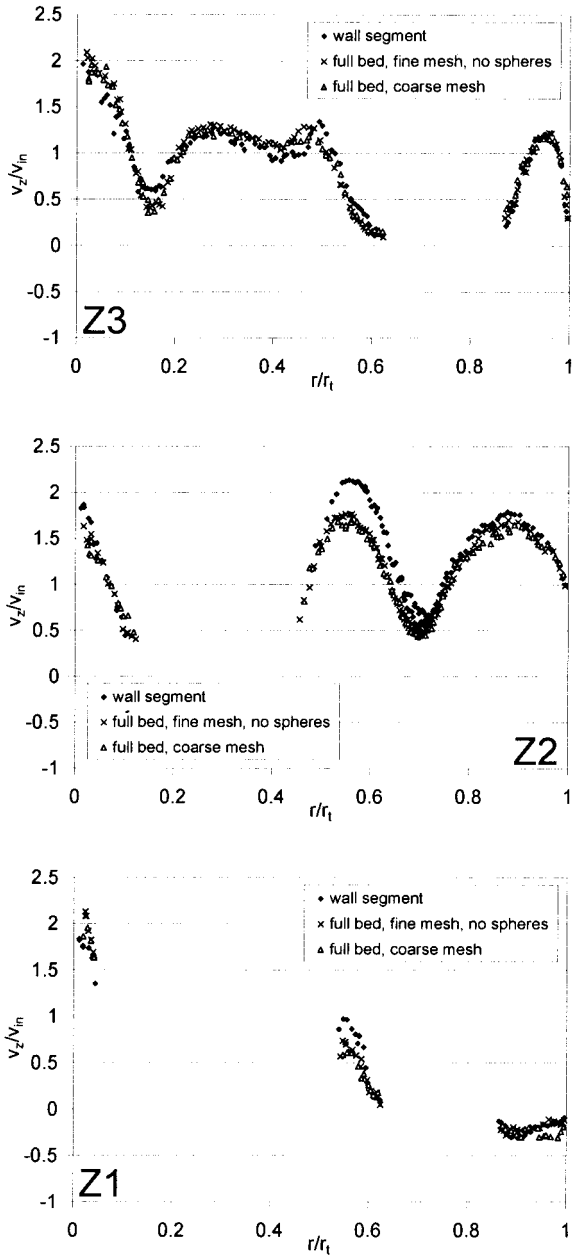

Figure 6. Comparison of axial velocity components at the three different axial positions in the wall segment and two full-bed geometries.

files. This confirms complete mesh independence of the wall-segment geometry, and proper resolution of the wall functions. Again, similar plots were made for the radial and tangential components of velocity, and again essentially the same results were obtained.

Correlation of Fluid Flow with Wall Heat Transfer

With the results of the wall-segment geometry validated, we can develop a methodology to relate the wall heat transfer to the near-wall flow features. This approach allows us to link the effectiveness of local heat transfer to the packing geometry, through the local flow features. This is an essential step in optimizing catalyst particle shape.

The structure of the packing next to the wall is shown in Figure 8. The ringlike structure of the near-wall packing was mentioned previously in discussing Figures 1 and 3. It is further clear from Figure 8 that the $N = 4$ sphere bed geometry shows a structured packing in the near-wall region. The packing of the spheres is very strongly influenced by the presence of the column wall, organizing the packing in the rings of nine spheres along the wall, as was described earlier. The flow solution obtained in the wall-segment model is superimposed on the bed structure in Figure 8, where pathlines are shown. We

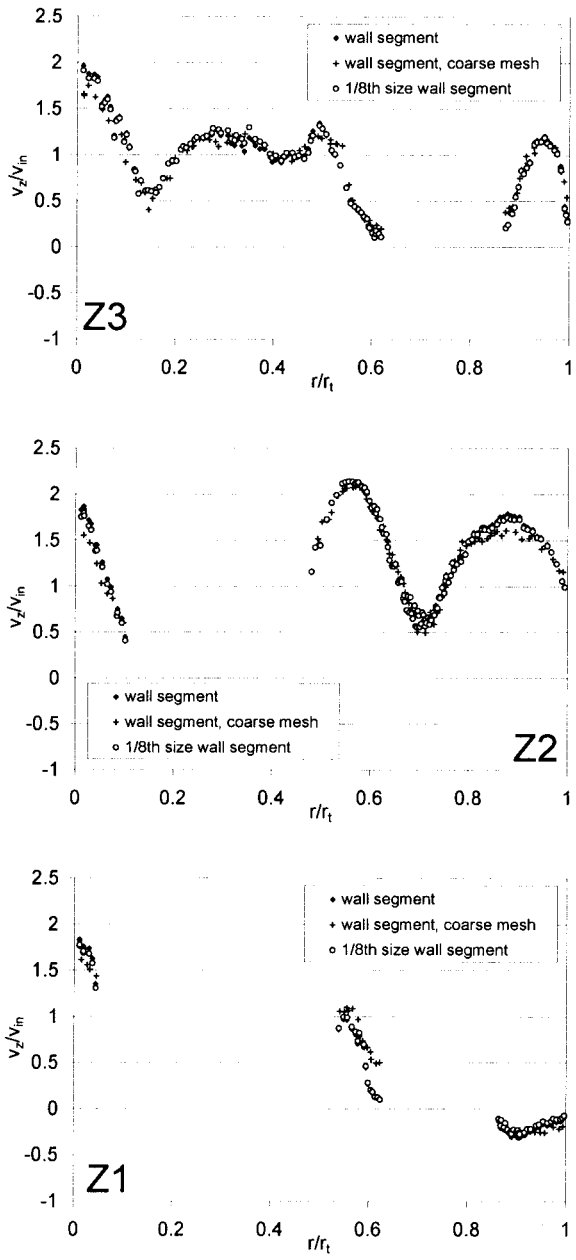

Figure 7. Comparison of axial velocity components at the three different axial positions in the wall segment geometries at two different mesh densities and 1/8th size.

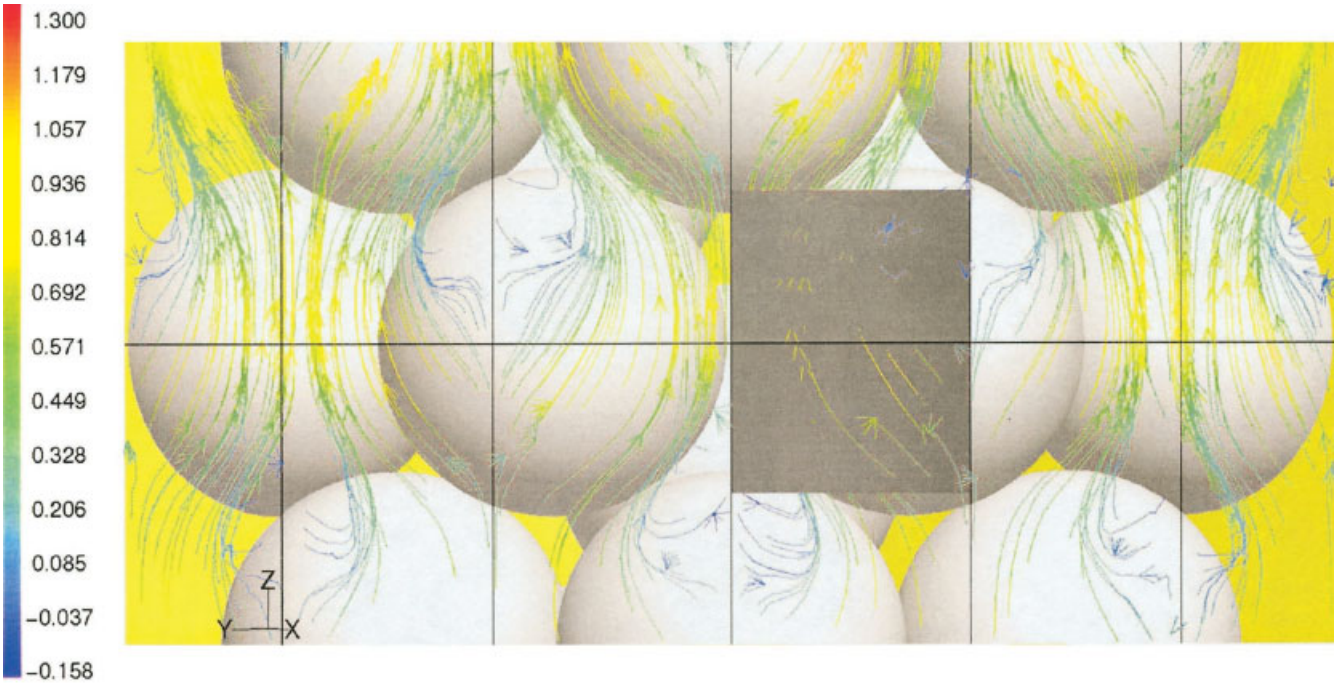

Figure 8. Parallel projection of the wall segment model, indicating the regularity of the wall structure.

can identify repetition in the flow field, directly related to the repetitive structure of the packing. Regions of fast axial flow between the spheres, and slow recirculating flow downstream of the wall–particle contact points are clearly seen. This repetitive structure allows us to concentrate on a smaller section of the geometry for the comparative study.

When we look at the heat flux map of the wall-segment cylindrical wall, as shown in Figure 9, we can also clearly

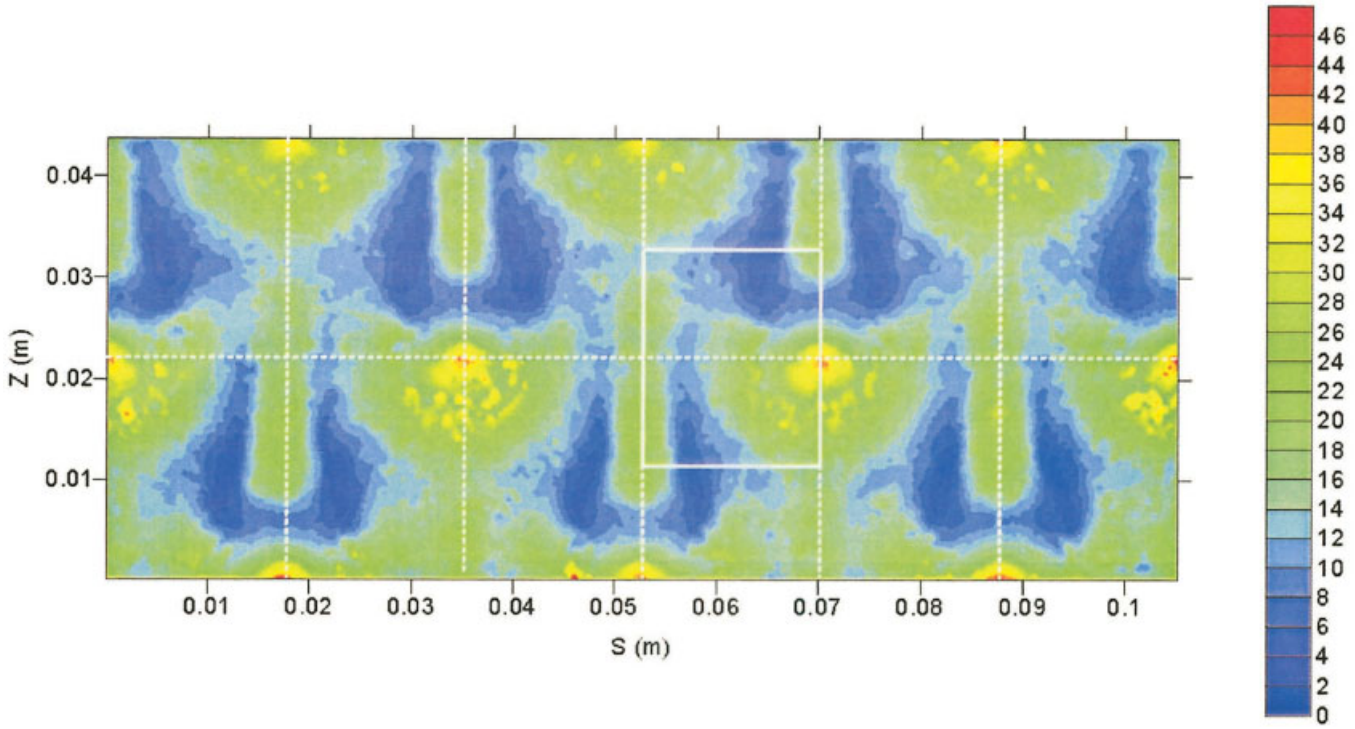

Figure 9. Wall heat flux map on the cylinder wall of the wall segment model, in kW/m^2.

The repetitive structure is indicated by the gridlines.

identify a repetitive structure in the heat flux pattern. The circular, red and yellow regions of high flux correspond to the contact points between the particles and the wall, where flow is almost stagnant. Around these points the fluid gap between particle and wall is very thin and the higher thermal conductivity of the alumina particles provides a pathway for good heat transfer. Just downstream of the contact points, we can identify "horseshoe"-shaped blue regions of lower heat flux. These correspond to regions where the gap between particle and wall is relatively wide, and the flow within the gap is slow and occasionally recirculating. The green regions of intermediate heat flux between the arms of the horseshoe correspond to regions of faster flow as the fluid is squeezed through narrow gaps between particles or between particle and wall. The broken lines indicate the unique elements in the repetitive structure. When we look at a similar picture of the geometric structure of the bed, as shown in Figure 8, we see that the repetitive structure of the heat flux map and the wall packing structure are related.

A small difference in aspect ratios of the same cylinder-wall plane can be noted between Figure 8 and Figure 9. This may be explained by the fact that Figure 9 was created using numerical data from the CFD simulation for which the 3-D coordinate data were transcribed to 2-D data to facilitate a 2-D plot, with the arc length s of the wall along the x-axis and the height of the wall along the y-axis. In contrast, Figure 8 displays an isometric parallel projection normal to the cylinder wall in the center of the arc length of the wall, resulting in a seemingly smaller arc length of the wall.

With the repetitive structure of the flow directly related to the wall packing structure and a similar apparent structure found in the wall heat flux map, we can try to quantitatively relate the flow structure to the wall heat flux in a repetitive element. The element chosen is indicated in Figure 8 by the gray box and in Figure 9 by the solid line box.

Statistical approach

Our initial hypothesis was that velocity components on a local level, on a scale of several control volumes, could be related to the local wall heat fluxes. It was expected that especially the radial components of velocity would have a distinct influence on the heat transfer processes. A procedure was developed, therefore, for quantitative analysis of any direct relation between the local velocity components and the local wall heat flux.

The object was to relate the local wall heat flux to the immediate neighboring fluid flow. The fluid flow in a small region close to the wall (up to about 5 mm away from the wall, 10% of the tube radius) was categorized by axial, radial, and tangential velocity components. Each component was then averaged over the region along the direction perpendicular to the tube wall, at each position on the wall. By organizing the data in this way, the fluid flow components could be directly related to the wall heat flux in the same region of the tube. The same procedure was followed for other attributes of the flow field, as discussed below.

Results are shown in Figure 10, for direct numerical comparisons of the local wall heat flux with the axial, radial, and tangential components of flow. The flow components are normalized using the local velocity magnitude. Figure 10 shows no obvious relation between wall heat flux and the immediate neighboring flow components. There is considerable spread in the data. The same value of wall heat flux can be obtained for very different values of a given velocity component, even for both positive and negative values. It can be concluded, however, that backflow (a negative v_z component) is associated with areas of low heat flux only. The highest wall heat fluxes appear only for strongly axially directed flows ($v_z/|v| \approx 1$), although the presence of such strong axial flows does not imply that wall heat flux will be high. Similarly, it can be concluded that in high heat flux areas radial flow tends to be positive (toward the wall) and in low heat flux areas it is mostly negative (away from the wall). Nothing can be said about the

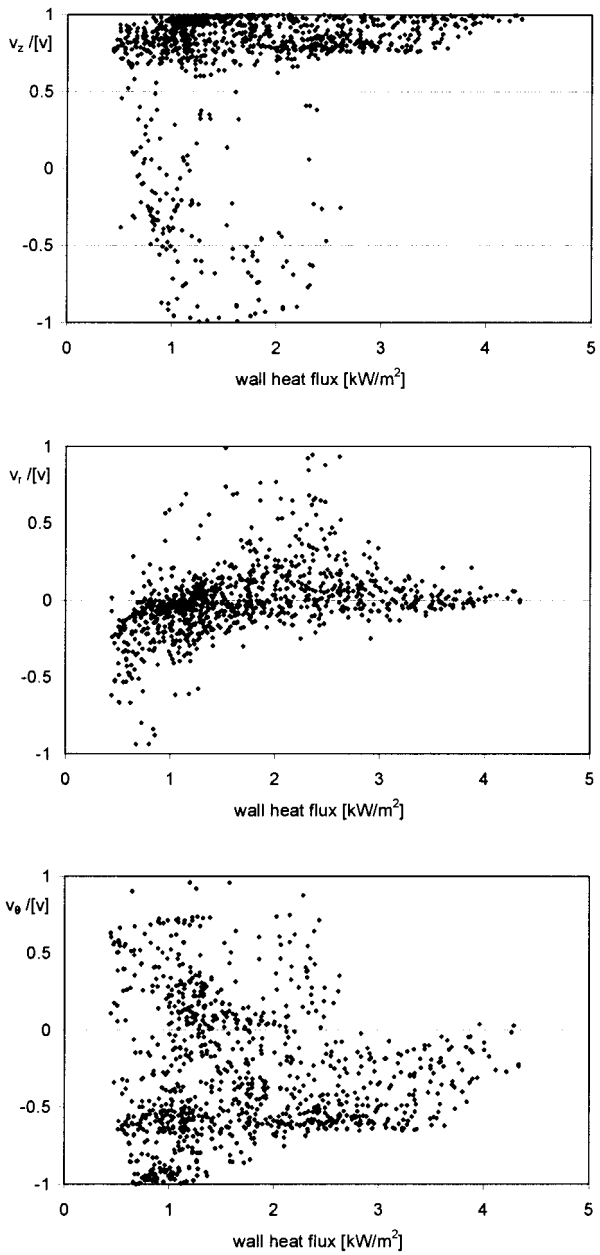

Figure 10. Normalized near-wall velocity components directly related to the local wall heat fluxes.

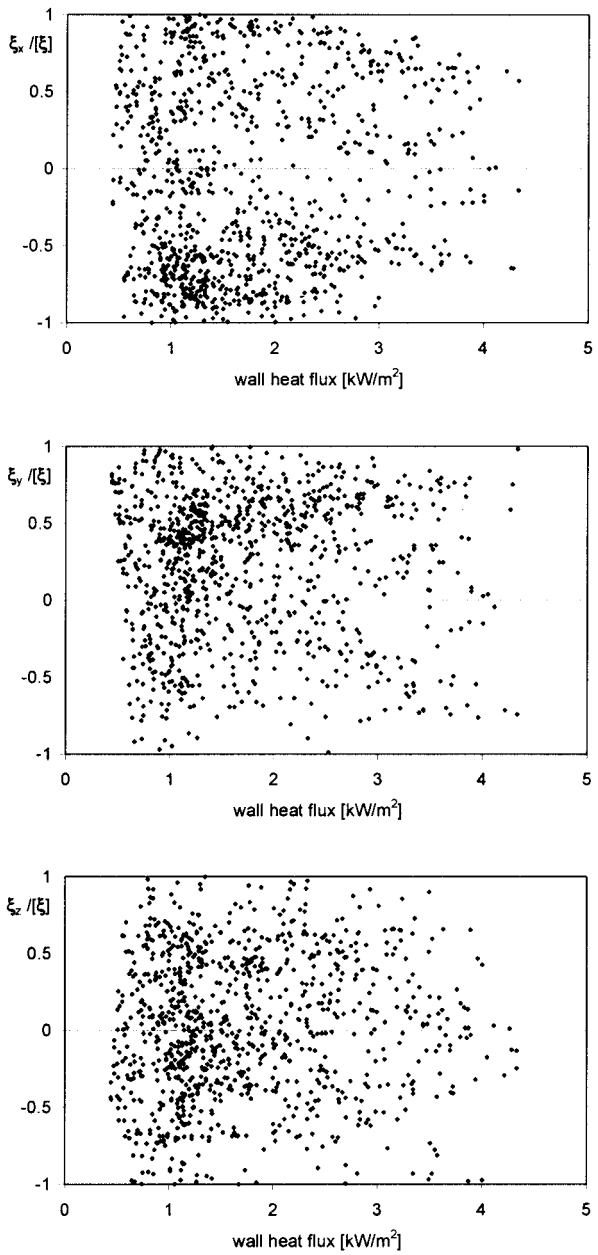

Figure 11. Normalized near-wall vorticity components directly related to the local wall heat fluxes.

angular velocity component. The indicated trends are tentative at best, although it was concluded that there was no clear, distinct relation between the local velocity components and the local wall heat flux.

It was next postulated that the vortices in the flow may have had an influence on the wall heat flux. This was motivated by the observation of poor heat transfer in the same regions as recirculating flow, in Figures 8 and 9. The vorticity of the flow $\boldsymbol{\xi}$ is a measure of the rotation of a fluid element as it moves in the flow field, and it is defined as the curl of the velocity vector, $\boldsymbol{\xi} = \nabla \times \boldsymbol{\nu}$. An identical comparison as was done with the velocity components was performed using the vorticity components in the flow. Figure 11 shows the direct comparisons between the normalized local vorticity components and the local wall heat fluxes. The vorticity components showed absolutely no correlation with the wall heat fluxes.

Another aspect of flow that was investigated was the flow helicity H. The flow helicity is defined as the dot product of vorticity and the velocity vector, $H = (\nabla \times \boldsymbol{\nu})\cdot\boldsymbol{\nu}$. The helicity of the flow combines the vorticity and the flow field; it provides insight into the vorticity aligned with the fluid stream. In the previous comparisons the relation between the velocity components and the heat flux was, although minimal, more prominent than the relation between the vorticity and the heat flux. By combining the velocity with the vorticity, we might get a better idea whether the vorticity plays a part in the local heat transfer process. As was expected from the definition of helicity, the data were more structured than was the case with the vorticity. There was still too much spread in the data; however, so as not to compose any strict relation between the local helicity and the local wall heat flux, the plots are not shown here.

Besides the twisting of the flow, described with the vorticity and the helicity, we inspected velocity component derivatives, and did a similar quantitative comparison. A relation might have been expected between the shear in the flow and the wall heat fluxes. In the simulation geometry the axial flow component is by far the dominant flow direction; in this comparison we looked at the derivative of the axial velocity component with respect to the three coordinates, r, θ, and z. The graphs in Figure 12 show the direct relation between the axial velocity component derivatives and the local wall heat flux. Similar to the previous comparisons there, again, was not an easily identifiable relation. The comparisons of the velocity component derivatives showed less spread than that in the comparisons against the vorticity or helicity.

In the comparison of the axial derivative of the axial velocity component against the wall heat flux in the top graph in Figure 12, most of the data showed a derivative value close to zero, meaning that there was not much acceleration or deceleration of the flow. From the comparison, we can draw some general conclusions, similar to the relations between the wall heat flux and the velocity components. Where dv_z/dz was positive, the flow was accelerating, or turning around from reverse flow to the main flow direction, and this occurred only in the low wall heat flux areas. The gradient dv_z/dz was negative in the medium flux area, most likely the area just downstream of the sphere-wall contact point where the axial component of the flow decreased, as it was diverted tangentially around the contact point.

The bottom two graphs in Figure 12 show the radial and tangential derivatives of the axial velocity component. The spread of the data in these comparisons, especially the radial derivative case, was considerable, and comparable to the amount encountered with the vorticity and helicity comparisons. The asymmetric picture seen for the tangential derivative in the bottom graph of Figure 12 was attributed to the choice of the repetitive area. Tangentially, the repetitive area was mirrored on either side of the tangential boundaries. In this case, therefore, the tangential derivative of the flow component showed data with mostly negative values; in the mirrored section on either side the data would be inverted, showing

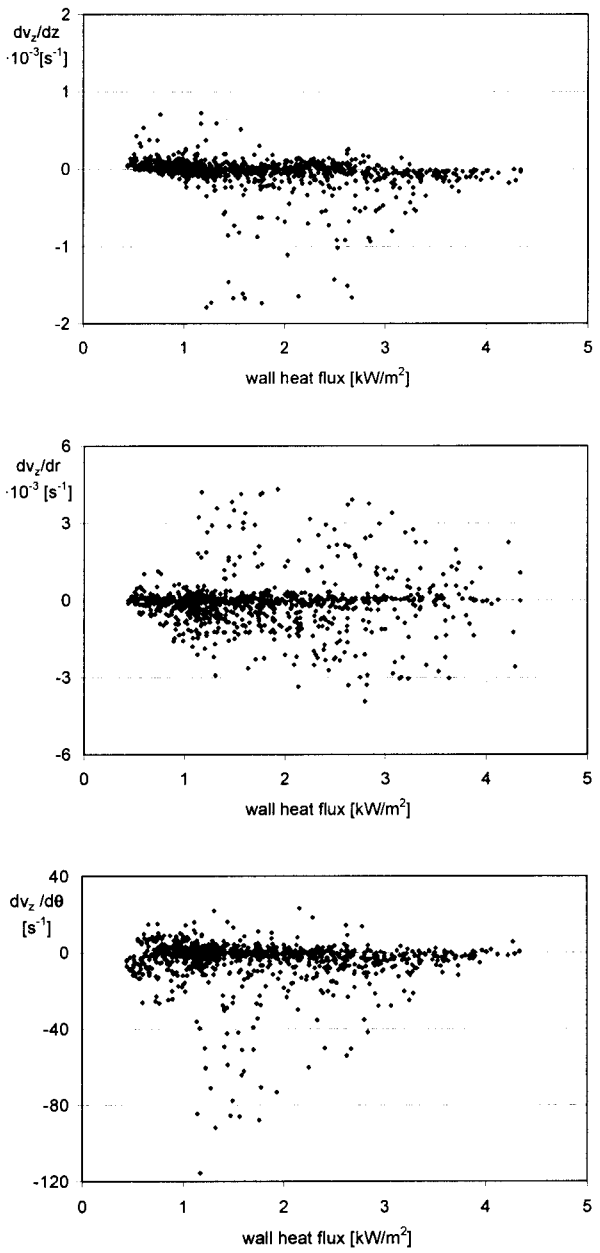

Figure 12. Near-wall partial velocity derivatives directly related to the local wall heat fluxes.

mostly positive values. For the tangential derivative of the axial velocity component, the more extreme values were found in the low flux areas and in the high flux area the derivative values were close to zero, similar to the axial derivative case.

From the numerical comparisons, it can be concluded that there appears to be no statistical relation between the local flow features and the wall heat flux. To determine the proper numerical representation of the flow field for making a direct quantitative comparison is a difficult task because it may not be the local flow behavior at the wall that defines the conditions locally, but a larger scale flow feature. It is often important to know the history of the local fluid, to understand its participation in the local heat transfer rate.

Conceptual approach

It was concluded that for a better understanding of the influence of the flow field on the wall heat flux, a more conceptual comparison was required. It was determined that we had to look at features of the flow on a larger scale than that used for the local analysis of the previous section. To do this, the flow field that was used to gather the data for the comparative plots in Figures 10–12 was reduced to a cartoon showing only the main flow features. This could then be related to a plot of the wall heat flux by conceptual comparison. In this way a simplified quantitative comparison is combined with an overall view of the situation allowing for a relation of the flow situation to the wall heat flux.

To illustrate this approach, the detailed flow field shown in Figure 13a was simplified and divided into several main features, as shown in Figure 13b. The main through-flow in the center of the section is indicated by a darker surface on the bottom of the section, flowing around the spherical particle, to the top of the section. In the wake area downstream of the sphere, there is a recirculating flow displaying both backflow (negative z velocities) and radial flow toward the wall. The third main feature is a radial flow in the left lower corner, which is part of the recirculating wake flow of a spherical particle located below the indicated section.

Figure 13c shows the wall heat flux in the part of the wall for which the outline is displayed in Figure 13a, and that constitutes the front surface in Figure 13b. As can be seen when the heat flux map is related to the basic flow features, there is no dominating flow direction that causes a higher or lower heat flux through the wall. The lower heat flux is located in the areas where recirculating flow and the main through-flow meet. These transition, or mixing regions are not identified by a particular flow direction, which explains why the plots in Figure 10 did not show a particular trend.

When the plots from Figure 10 are related to the conceptual comparison from Figure 13 it can be seen that the fact that backflow was seen only in low wall heat flux areas is related to the fact that backflow occurs only in the sphere wakes, which are an essential part of the flow-mixing regions. Similarly the negative radial velocities are limited to low flux areas, and are specifically located in the wake flow, near the mixing area in the top right hand corner of the segment.

Conclusions

Computational fluid dynamics was applied for the first time to the detailed 3-D analysis of simultaneous flow and heat transfer through realistic spherical packings in the wall region of a fixed-bed reactor tube. It was shown, for $N = 4$, that flow simulation in a flow-periodic wall segment gave the same results as the simulation of a full bed, when the proper symmetry boundary conditions were applied. It was demonstrated that the identification and isolation of a typical portion of the bed could be used to reduce the computational burden of these simulations when the main focus is on near-wall phenomena.

Maps of local wall heat flux were obtained for a constant wall temperature tube, showing the pattern of wall heat flux corresponding to the local bed structure. Experimental techniques to date have not been able to give such detailed local heat transfer properties. The patterns showed the strong point-

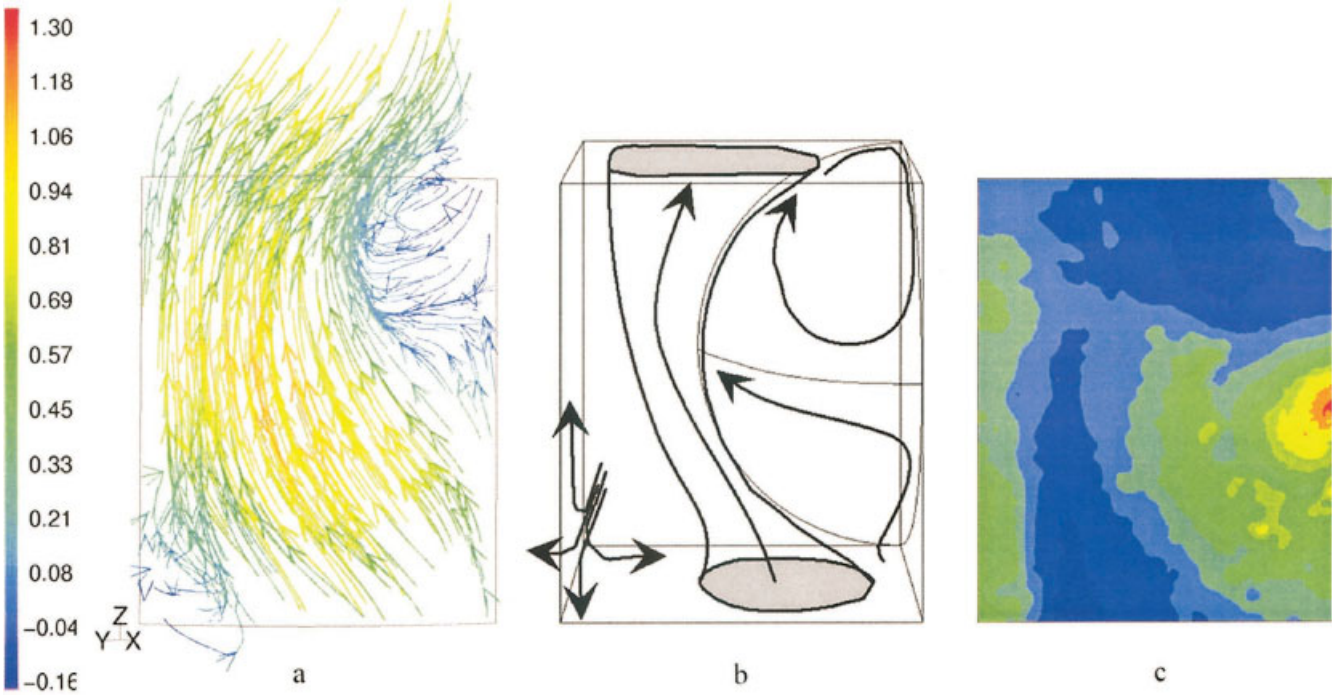

Figure 13. The unit-cell section used for comparing fluid flow to wall heat flux: (a) the flow field expressed in pathlines; (b) the simplified expression of the flow field in the fluid section; (c) relative wall heat flux.

The viewpoint here is that of an observer located on the tube wall.

wise variation of local wall heat flux, which had not been suggested previously.

A reasonable hypothesis was tested, that the local wall heat flux would correlate with measures of the local flow field. Somewhat surprisingly, no such correlation could be found for the fairly wide range of measures that we tested. Our interpretation of the results was that to be able to relate a near-wall flow field to a wall heat flux pattern, both a quantitative analysis and a conceptual analysis are required. The quantitative analysis shows which flow components are involved in low or high wall heat flux, although, without the conceptual analysis, it is impossible to explain with which flow feature the flow component is associated. Because basic flow components, such as flow direction or magnitude, are not exclusive to certain flow features, it is impossible to identify causal relations in a quantitative analysis alone. The conceptual analysis suggests that the wall heat flux at a particular position is part of a larger pattern of heat flux, which is related to the patterns of fluid flow on the scale of a particle or larger.

The sphere-packed bed, showing a repetitive packing structure, facilitated the comparison of heat-transfer data and flow field on a local unit cell level. To be able to make more general conclusions about the effects that the features of the flow field have on the near-wall heat transfer, it would be necessary to compare a wider range of flow fields and bed structures. The sphere-packed beds are limited in the types of near-wall packing features that they can display. The logical expansion of the present work would be to different catalyst particle geometries. Our subsequent results on the influences of nonspherical catalyst particle geometry on fixed-bed near-wall heat transfer will be presented in a future publication. Successful identification of links between particle geometry, near-wall fluid flow, and wall heat flux should enable design of catalyst particles that are more effective for heat transfer in fixed beds.

Acknowledgments

The authors thank Johnson Matthey Catalysts, and the DuPont Educational Fund for their financial support. Also, Fluent, Inc., is acknowledged for the university license of their CFD software.

Literature Cited

Bey, O., and G. Eigenberger, "Fluid Flow through Catalyst Filled Tubes," *Chem. Eng. Sci.,* **52**, 1365 (1997).

Bode, J. "Computational Fluid Dynamics Applications in the Chemical Industry," *Comp. Chem. Eng. Suppl.*, **18**, S247 (1994).

Calis, H. P. A., J. Nijenhuis, B. C. Paikert, F. M. Dautzenberg, and C. M. van den Bleek, "CFD Modeling and Experimental Validation of Pressure Drop and Flow Profile in a Novel Structured Catalytic Reactor Packing," *Chem. Eng. Sci.*, **56**, 1713 (2001).

Dalman, M. T., J. H. Merkin, and C. McGreavy, "Fluid Flow and Heat Transfer Past Two Spheres in a Cylindrical Tube," *Computers and Fluids*, **14**, 267 (1986).

Debus, C., H. Nirschl, A. Delgado, and V. Denk, "Numerische Simulation des lokalen Impulsaustausches in Kugelschüttungen," *Chem.-Ing.-Tech.*, **70**, 415 (1998).

Derkx, O. R., and A. G. Dixon, "Determination of the Fixed Bed Wall Heat Transfer Coefficient Using Computational Fluid Dynamics," *Numerical Heat Transfer A*, **29**, 777 (1996).

Dixon, A. G., and M. Nijemeisland, "CFD as a Design Tool for Fixed-Bed Reactors," *Ind. Eng. Chem. Res.*, **40**, 5246 (2001).

Esterl, S., C. Debus, H. Nirschl, and A. Delgado, "Three-Dimensional Calculations of the Flow Through Packed Beds," in *ECCOMAS 98*, K. D. Papailiou, ed., pp. 692–696. 4th Eur. Comput. Fluid Dyn. Conf., Wiley, New York (1998).

Fluent/UNS 4.2 User Guide, Fluent Inc., Lebanon, NH (1997).

Freund, H., T. Zeiser, F. Huber, E. Klemm, G. Brenner, F. Durst, and G. Emig, "Numerical Simulations of Single Phase Reacting Flows in Ran-

domly Packed Fixed-Bed Reactors and Experimental Validation," *Chem. Eng. Sci.*, **58**, 903 (2003).
Georgiadis, J., D. R. Noble, M. R. Uchanski, and R. O. Buckius, "Questions in Fluid Mechanics. Tortuous Micro-flow in Large Disordered Packed Beds," *ASME J. Fluid Eng.*, **118**, 434 (1996).
Giese, M., K. Rottschäfer, and D. Vortmeyer, "Measured and Modeled Superficial Flow Profiles in Packed Beds with Liquid Flow," *AIChE J.*, **44**, 484 (1998).
Harris, C. K., D. Roekaerts, F. J. J. Rosendal, F. G. J. Buitendijk, Ph. Daskopoulos, A. J. N. Vreenegoor, and H. Wang, "Computational Fluid Dynamics for Chemical Reactor Engineering," *Chem. Eng. Sci.*, **51**, 1569 (1996).
Jakobsen, H. A., H. Lindborg, and V. Handeland, "A Numerical Study of the Interactions between Viscous Flow, Transport and Kinetics in Fixed Bed Reactors," *Comput. Chem. Eng.*, **26**, 333 (2002).
Kays, W. M. "Turbulent Prandtl Number—Where Are We?" *J. Heat Transfer*, **116**, 284 (1994).
Kim, S.-E., and D. Choudhury, "A Near-Wall Treatment Using Wall Functions Sensitized to Pressure Gradient," in *ASME FED*, **217**, *Separated and Complex Flows*, ASME (1995).
Kuipers, J. A. M., and W. P. M. van Swaaij, "Computational Fluid Dynamics Applied to Chemical Reaction Engineering," *Adv. Chem. Eng.*, **24**, 227 (1998).
Launder, B. E., and D. B. Spalding, "The Numerical Computation of Turbulent Flows," *Comp. Methods Appl. Mech. Eng.*, **3**, 269 (1974).
Lloyd, B., and R. Boehm, "Flow and Heat Transfer Around a Linear Array of Spheres," *Numerical Heat Transfer*, **26**, 237 (1994).
Logtenberg, S. A., and A. G. Dixon, "Computational Fluid Dynamics Studies of Fixed Bed Heat Transfer," *Chem. Eng. Process.*, **37**, 7 (1998a).
Logtenberg, S. A., and A. G. Dixon, "Computational Fluid Dynamics Studies of the Effects of Temperature-Dependent Physical Properties on Fixed-Bed Heat Transfer," *Ind. Eng. Chem. Res.*, **37**, 739 (1998b).
Logtenberg, S. A., M. Nijemeisland, and A. G. Dixon, "Computational Fluid Dynamics Simulations of Fluid Flow and Heat Transfer at the Wall-Particle Contact Points in a Fixed-Bed Reactor," *Chem. Eng. Sci.*, **54**, 2433 (1999).
Maier, R. S., D. M. Kroll, Y. E. Kutsovsky, H. T. Davis, and R. S. Bernard, "Simulation of Flow through Bead Packs Using the Lattice Boltzmann Method," *Phys. Fluids*, **10**, 60 (1998).
Manz, B., L. F. Gladden, and P. B. Warren, "Flow and Dispersion in Porous Media: Lattice-Boltzmann and NMR Studies," *AIChE J.*, **45**, 1845 (1999).
McKenna, T. F., R. Spitz, and D. Cokljat, "Heat Transfer from Catalysts with Computational Fluid Dynamics," *AIChE J.*, **45**, 2392 (1999).
Mueller, G. E. "Numerical Simulation of Packed Beds with Monosized Spheres in Cylindrical Containers," *Powder Technol.*, **92**, 179 (1997).
Nijemeisland, M., and A. G. Dixon, "Comparison of CFD Simulations to Experiment for Convective Heat Transfer in a Gas-Solid Fixed Bed," *Chem. Eng. J.*, **82**, 231 (2001).
Nirschl, H., H. A. Dwyer, and V. Denk, "Three-Dimensional Calculations of the Simple Shear Flow around a Single Particle between Two Moving Walls," *J. Fluid Mechanics*, **283**, 273 (1995).
Patankar, S. V. *Numerical Heat Transfer and Fluid Flow*, Hemisphere, Washington, DC (1980).
Petre, C. F., F. Larachi, I. Iliuta, and B. P. A. Grandjean, "Pressure Drop through Structured Packings: Breakdown into the Contributing Mechanisms by CFD Modeling," *Chem. Eng. Sci.*, **58**, 163 (2003).
Ranade, V. *Computational Flow Modeling for Chemical Reactor Engineering*, Academic Press, New York (2002).
Sørensen, J. P., and W. E. Stewart, "Computation of Forced Convection in Slow Flow through Ducts and Packed Beds. III. Heat and Mass Transfer in a Simple Cubic Array of Spheres," *Chem. Eng. Sci.*, **29**, 827 (1974).
Suekane, T., Y. Yokouchi, and S. Hirai, "Inertial Flow Structures in a Simple-Packed Bed of Spheres," *AIChE J.*, **49**, 10 (2003).
Winterberg, M., E. Tsotsas, A. Krischke, and D. Vortmeyer, "A Simple and Coherent Set of Coefficients for Modelling of Heat and Mass Transport with and without Chemical Reaction in Tubes Filled with Spheres," *Chem. Eng. Sci.*, **55**, 967 (2000).
Yakhot, V., and S. A. Orszag, "Renormalization Group Analysis of Turbulence. I. Basic Theory," *J. Sci. Computing*, **1**, 1 (1986).
Yuen, E. H. L., A. J. Sederman, F. Sani, P. Alexander, and L. F. Gladden, "Correlations between Local Conversion and Hydrodynamics in a 3-D Fixed-Bed Esterification Process: An MRI and Lattice-Boltzmann Study," *Chem. Eng. Sci.*, **58**, 613 (2003).
Zeiser, T., P. Lammers, E. Klemm, Y. W. Li, J. Bernsdorf, and G. Brenner, "CFD-Calculation of Flow, Dispersion and Reaction in a Catalyst Filled Tube by the Lattice Boltzmann Method," *Chem. Eng. Sci.*, **56**, 1697 (2001).
Zeiser, T., M. Steven, H. Freund, P. Lammers, G. Brenner, F. Durst, and J. Bernsdorf, "Analysis of the Flow Field and Pressure Drop in Fixed Bed Reactors with the Help of Lattice Boltzmann Simulations," *Philos. Trans. R. Soc. Lond. A*, **360**, 507 (2002).

Manuscript received Mar. 17, 2003, revision received Aug. 27, 2003, and final revision received Oct. 10, 2003.